APPLIED PHYSICS

Chemiluminescence resonance energy transfer–based nanoparticles for quantum yield–enhanced cancer phototheranostics

Jueun Jeon[1]*, Dong Gil You[1]*, Wooram Um[2], Jeongjin Lee[2], Chan Ho Kim[1], Sol Shin[2], Seunglee Kwon[1], Jae Hyung Park[1,2,3†]

Chemiluminescence (CL) has recently gained attention for CL resonance energy transfer (CRET)–mediated photodynamic therapy of cancer. However, the short duration of the CL signal and low quantum yield of the photosensitizer have limited its translational applications. Here, we report CRET-based nanoparticles (CRET-NPs) to achieve quantum yield–enhanced cancer phototheranostics by reinterpreting the hidden nature of CRET. Owing to reactive oxygen species (ROS)–responsive CO_2 generation, CRET-NPs were capable of generating a strong and long-lasting photoacoustic signal in the tumor tissue via thermal expansion–induced vaporization. In addition, the CRET phenomenon of the NPs enhanced ROS quantum yield of photosensitizer through both electron transfer for an oxygen-independent type I photochemical reaction and self-illumination for an oxygen-dependent type II photochemical reaction. Consequently, owing to their high ROS quantum yield, CRET-NPs effectively inhibited tumor growth with complete tumor growth inhibition in 60% of cases, even with a single treatment.

INTRODUCTION

Chemiluminescence (CL) resonance energy transfer (CRET) refers to a nonradiative transfer mechanism between CL donors and adjacent acceptors, usually located within 10 nm (*1*–*3*). Geared by nanotechnology, various CRET systems have been rationally designed and have led to remarkable advances in the field of molecular imaging (*4*–*6*). In particular, reactive oxygen species (ROS) that are representative traces of inflammatory diseases were first visualized by CL imaging involving CRET (*1*). Although CL image quality has been recognized as superior to that of conventional fluorescence imaging in terms of specificity and signal-to-noise ratio (*7*, *8*), long-term in vivo ROS imaging remains challenging in the field due to the short duration of CL signals (*6*, *9*, *10*).

Photoacoustic (PA) imaging has emerged as a promising modality for continuous and repetitive monitoring of pathologic sites, on the basis of the beneficial features of both well-established optical and ultrasound (US) imaging: noninvasiveness, cost-effectiveness, and real-time scanning (*11*, *12*). This imaging technique typically relies on optically excited contrast agents, generating US signals via thermal expansion or vaporization (*13*, *14*). Although the former is biologically safer, the resulting PA signal intensity is much lower than that achieved by the latter (*14*, *15*). Recently, thermal expansion–induced vaporization (TEIV) has been investigated with perfluorocarbon (PFC) and plasmonic nanoparticles (NPs) to generate safe and effective PA signals (*15*). However, such PFC-based imaging systems are innately inadequate for disease-specific molecular imaging. On the other hand, CRET systems, composed of peroxalate and fluorescent dye, specifically generate carbon dioxide (CO_2) in response to hydrogen peroxide (H_2O_2) (*16*), the most abundant ROS at tumor sites (*17*). Despite the ideal properties of such CRET systems, they have never been adopted for tumor site–specific PA imaging through TEIV.

Because the CRET-based NPs (CRET-NPs) are capable of delivering photosensitizers, their application has not been limited to molecular imaging, with rapid expansion to cancer phototherapy (*18*). In conventional photodynamic therapy (PDT) of cancer, poor in vivo penetration depth of external light to activate photosensitizers is a common limitation (*17*, *18*). Although self-illuminating NPs based on CRET have been intensively explored to address this problem, the results were insufficient to reach significant therapeutic outcomes (*10*, *19*, *20*). Therefore, much effort has been devoted to improving the ROS quantum yield of a photosensitizer for effective PDT (*18*, *21*). For instance, chelation of heavy metals, including Pt, Au, and Ag, has been demonstrated to enhance spin-orbit coupling of the photosensitizer and increase the intersystem crossing rate (*22*–*24*), leading to an elevated single oxygen ($^1O_2$) quantum yield via the type II photochemical reaction (*24*). The traditional photosensitizers, however, are not effective for the hypoxic region in tumor tissue, owing to oxygen dependency of the type II photoreaction (*25*). Thus, there is a need to develop strategies to enhance ROS quantum yield in an oxygen-independent manner for widespread use of cancer PDT in the clinic.

To address the aforementioned challenges in cancer phototheranostics, we prepared CRET-NPs by physically encapsulating a CL donor, bis[3,4,6-trichloro2-(pentyloxycarbonyl)phenyl]oxalate (TCPO), into self-assembled NPs composed of PEGylated carboxymethyl dextran (PEG-CMD) as the hydrophilic shell and chlorin e6 (Ce6) as the hydrophobic CL acceptor (Fig. 1). When these NPs reach H_2O_2-rich tumor sites, TCPOs are rapidly oxidized to 1,2-dioxetanedione intermediates that are subsequently decomposed into CO_2 (*16*). Upon pulsed laser irradiation, the CO_2 can be vaporized by thermal expansion of Ce6 to amplify the PA signal (*26*). The H_2O_2-triggered CRET phenomenon also leads to electron transfer from TCPO to Ce6 and self-illumination within the CRET-NPs

[1]School of Chemical Engineering, College of Engineering, Sungkyunkwan University, 2066 Seobu-ro, Jangan-gu, Suwon 16419, Republic of Korea. [2]Department of Health Sciences and Technology, SAIHST, Sungkyunkwan University, 81 Irwon-ro, Gangnam-gu, Seoul 06351, Republic of Korea. [3]Biomedical Institute for Convergence at SKKU (BICS), Sungkyunkwan University, 2066 Seobu-ro, Jangan-gu, Suwon 16419, Republic of Korea.
*These authors contributed equally to this work.
†Corresponding author. Email: jhpark1@skku.edu

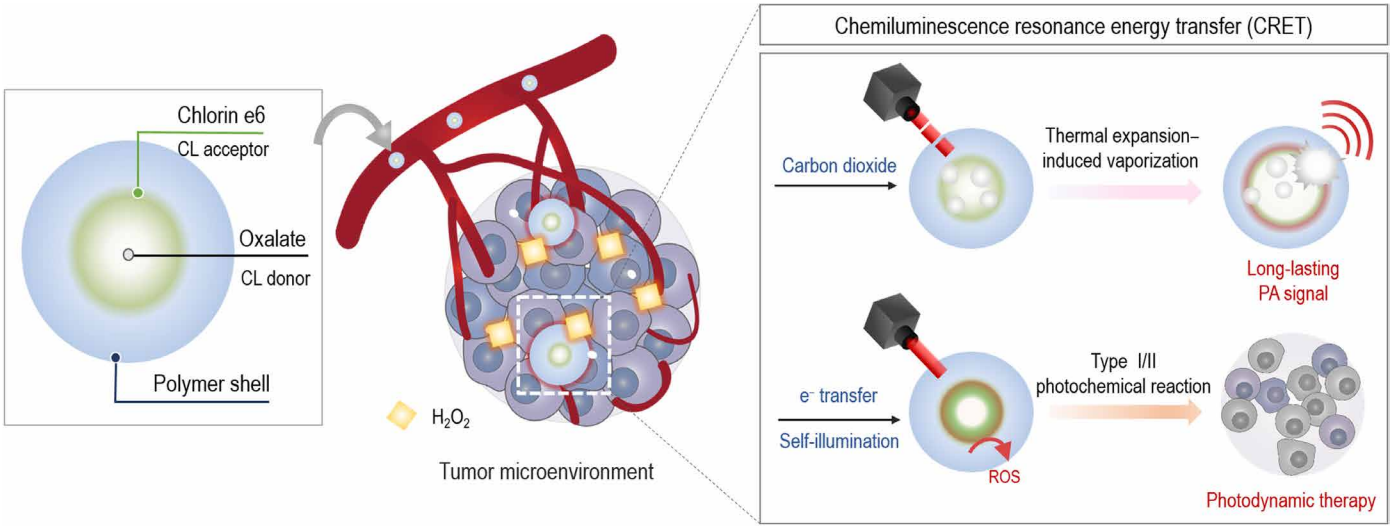

Fig. 1. Schematic illustration of CRET-NPs for cancer phototheranostics. CRET-NPs with a high ROS quantum yield can generate an intense PA signal by thermal expansion–induced vaporization. Because of its ROS-responsive CO_2 production, the strong PA signal of CRET-NPs can be generated at the tumor tissue for a long period of time. In addition, the CRET phenomenon of NPs enhances the ROS quantum yield through both electron transfer in the oxygen-independent type I photochemical reaction and self-illumination in the oxygen-dependent type II photochemical reaction.

(*27*). On the basis of these findings, we hypothesized that peroxalate/photosensitizer-based CRET-NPs could be long-acting cancer phototheranostic agents, allowing effective PA imaging and PDT by the following feasible mechanisms: PA signal improvement via TEIV and ROS quantum yield enhancement through both type I and type II photochemical reactions, respectively.

RESULTS

Synthesis and characterization of CRET-NPs

An amphiphilic polymer conjugate (PEG-CMD-Ce6), capable of being self-assembled into NPs in an aqueous condition, was prepared by chemical modification of PEG-CMD with Ce6 via formation of ester linkages (fig. S1). The chemical structure of the conjugate was confirmed using ^{1}H nuclear magnetic resonance (NMR) (fig. S2). We synthesized the PEG-CMD-Ce6 conjugate bearing 7.2 Ce6 molecules per 100 sugar units of CMD. Owing to its amphiphilic nature, PEG-CMD-Ce6 formed self-assembled NPs (Ce6-NPs) with a hydrodynamic size of 117.3 ± 8.84 nm and zeta potential value of −25.1 ± 0.71 mV. The Ce6-NPs had a unimodal size distribution and spherical shape in an aqueous condition (fig. S3). An H_2O_2-responsive CL donor, TCPO, was physically encapsulated into the Ce6-NPs using an oil-in-water emulsion method. The physicochemical properties of CRET-NPs are shown in Fig. 2. The CRET-NPs (128.5 ± 7.48 nm in diameter) had a unimodal size distribution and spherical shape in an aqueous condition (Fig. 2, A and B). As shown in Fig. 2C, with energy-dispersive x-ray spectroscopy (EDS) mapping images of CRET-NPs, the chlorine element of TCPO was colocalized with the nitrogen element of Ce6, suggesting that TCPOs were evenly loaded into Ce6-NPs. We then evaluated the stability of CRET-NPs by measuring particle size as a function of time, which is important in the CRET phenomenon between CL donor and acceptor. There were no significant changes in size of CRET-NPs for at least 7 days in phosphate-buffered saline (PBS; pH 7.4), even in the presence of 100 μM H_2O_2 (fig. S8). In addition, CRET-NPs were highly stable in standard simulated body fluid and fetal bovine serum (FBS)–containing PBS (pH 7.4) for 24 hours.

For CRET-NPs, a strong CL signal was observed in the presence of H_2O_2, whereas no signals were detected in the absence of TCPO and/or H_2O_2, indicating that CRET-NPs were highly responsive to H_2O_2 (Fig. 2D). To evaluate the wavelength of emitted light from the CRET-NPs, CL signals of CRET-NPs were observed using emission filters at the wavelength range of 520 to 845 nm (Fig. 2E). CRET-NPs showed a strong CL signal by CRET at 670 nm, the excitation wavelength of Ce6, implying that the emitted CL can activate Ce6 to produce $^1O_2$ molecules. To confirm the CRET phenomenon at the electron level, we assessed the electron fields of CRET-NPs and Ce6-NPs in the presence of H_2O_2. For both NPs, differential phase contrast (DPC) images revealed the presence of electron fields as bright and dark patches inside the nanostructure (Fig. 2F). We then obtained vector images of electron fields from DPC images. These Ronchigrams demonstrated that the electron field of CRET-NPs was stronger than that of Ce6-NPs. The intense electron field vectors of CRET-NPs were formed in larger and more diverse directions than those of Ce6-NPs. This electron transfer from the 1,2-dioxetanedione intermediate to the CL acceptor represents strong evidence of the CRET phenomenon.

CRET-NPs as a PA signal amplifier

Although conventional CRET-NPs have been extensively used for in vivo ROS imaging, the short duration of CL signals has limited their extended application in the clinic. In this study, we investigated the potential of TCPO/Ce6-based CRET-NPs as a PA signal amplifier for a prolonged period of time, because they can generate CO_2 molecules in a sustained manner in the presence of H_2O_2, followed by TEIV to enhance the PA signal (Fig. 3, A and B). As shown in Fig. 3C, for TCPO-bearing NPs, a quantity of CO_2 gas was produced for at least 24 hours in the presence of H_2O_2. To observe thermal expansion behavior, we then evaluated the photothermal effects of CRET-NPs by monitoring temperature change, in which CRET-NP

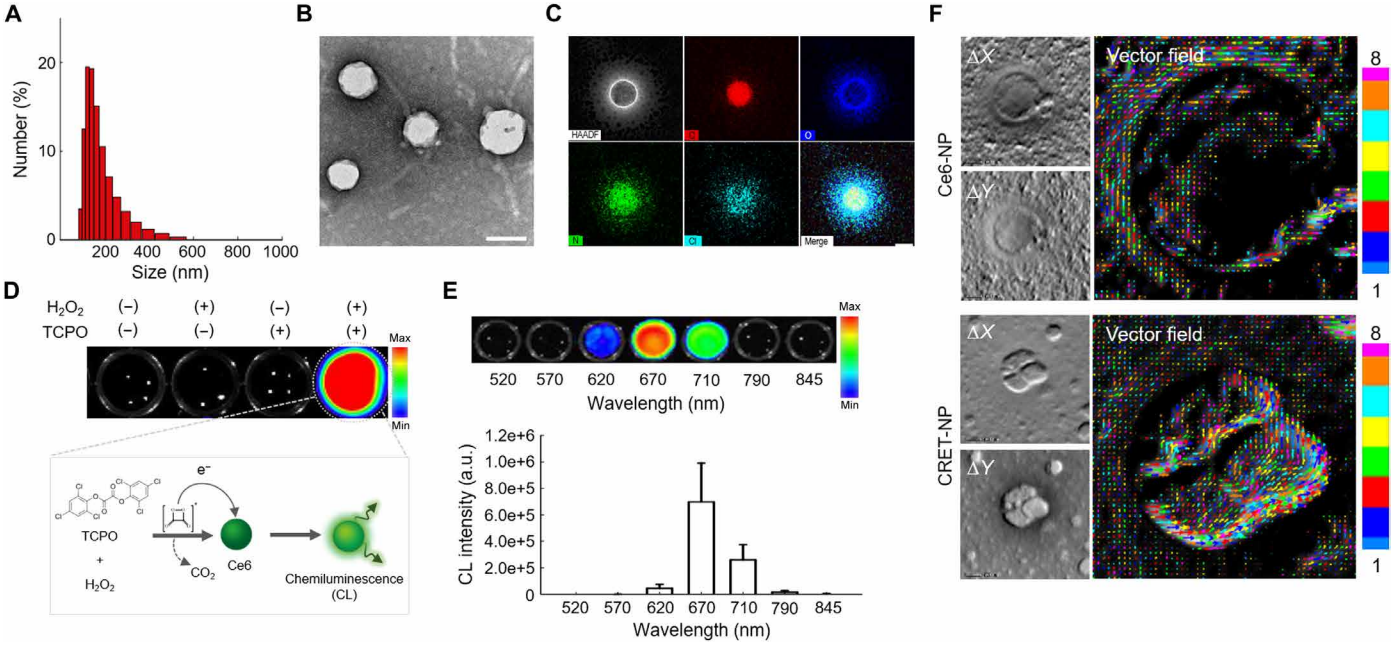

Fig. 2. Physicochemical characteristics of CRET-NPs. (**A**) Size distribution of CRET-NPs. (**B**) TEM image of CRET-NPs. (**C**) EDS mapping of CRET-NPs. Atomic distribution shows colocalization of TCPO and Ce6 in the particle cores. Scale bar, 100 nm. (**D**) CL images of CRET-NPs in the presence of TCPO and/or H_2O_2. (**E**) CL images of CRET-NPs in the presence of H_2O_2 at different wavelengths of emission filter (top). Quantification of the CL signal from CRET-NPs (bottom). Error bars represent the SD ($n = 3$). a.u., arbitrary units. (**F**) DPC images (left) and vector field images (right) of Ce6-NPs and CRET-NPs. The vector field images through the Ronchigram show the presence and direction of electrons in the CRET-NPs.

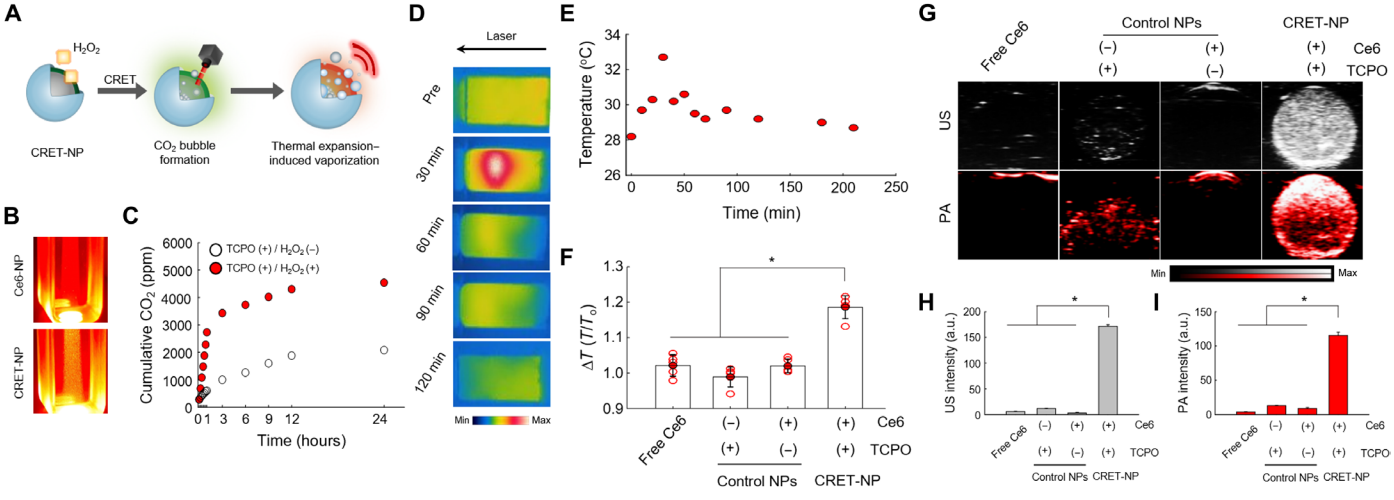

Fig. 3. TEIV behavior of CRET-NPs as the PA contrast agent. (**A**) Schematic illustration of TEIV by CRET-NPs. (**B**) Photographs of Ce6-NPs and CRET-NPs. In the presence of H_2O_2, CRET-NPs generated a quantity of CO_2 molecules. (**C**) Quantification of CO_2 molecules in the presence or absence of H_2O_2. (**D**) In vitro thermography of CRET-NPs under laser irradiation. (**E**) Thermal heating curve of CRET-NPs as a function of laser irradiation time. (**F**) Photothermal effects of free Ce6, TCPO-bearing NP, Ce6-NP, and CRET-NPs (left to right). The *y* axis represents the ratio of initial temperature to maximum temperature. Error bars represent the SD ($n = 5$). *$P < 0.0001$, analyzed by one-way analysis of variance (ANOVA). (**G**) In vitro US and PA imaging of free Ce6, TCPO-bearing NP, Ce6-NP, and CRET-NPs (left to right). (**H**) Comparison of US intensities and (**I**) PA intensities for free Ce6, TCPO-bearing NP, Ce6-NP, and CRET-NPs. Error bars represent the SD ($n = 3$). *$P < 0.0001$, analyzed by one-way ANOVA.

solution was exposed to a laser at a power density of 50 mW/cm^2 as the PA laser-mimetic condition. According to photothermal images, temperature reached the maximum value in 30 min, followed by a gradual decrease to ambient temperature (Fig. 3D). Quantitatively, the temperature of the CRET-NP solution increased from 28.2°C to 32.7°C at 30 min (Fig. 3E). On the other hand, PBS, Ce6-NPs, and TCPO-bearing NPs showed poor photothermal effects, with a temperature increase less than 5% (Fig. 3F). These photothermal effects of CRET-NPs, induced by thermal expansion of Ce6, may lead to vaporization of CO_2 to enhance PA quantum yield. The TEIV properties

of CRET-NPs were investigated in an agar-gel phantom (Fig. 3, G to I). Free Ce6 and Ce6-NPs did not exhibit a US or PA signal because they could not generate CO_2 as the thermal energy acceptor. In addition, TCPO-bearing NPs displayed a limited PA signal because there was no Ce6 as the thermal energy donor for CO_2 vaporization by thermal expansion. A strong PA signal was observed in CRET-NPs by H_2O_2-responsive TEIV, in which the PA signal intensity of CRET-NPs was 13- and 9-fold higher than those of Ce6-NPs and TCPO-bearing NPs, respectively.

CRET-NPs as a ROS-specific PA contrast agent in vivo

To compare the duration of the PA signal with that of the CL signal, CRET-NPs (in 100 μM H_2O_2) were subcutaneously injected into the lower backs of BALB/c nude mice. PA images were then collected as a function of time (fig. S9). The PA signal was detected for 24 hours, with an intensity that initially increased for 3 hours and then gradually decreased for the remaining period of time tested. These results suggest that CRET-NPs exhibited enhanced PA quantum yield by responding to H_2O_2 via TEIV. We then investigated the in vivo durability of CRET-NPs as a ROS-specific CL imaging agent using an optical imaging system after subcutaneous injection into the mice (Fig. 4A and fig. S10). As expected, a strong CL signal was observed in the lower back of the BALB/c nude mouse treated with CRET-NPs, whereas there was no detectable signal for the mouse with Ce6-NPs. After the CL signal of CRET-NPs reached the maximum intensity at 2 min, it rapidly decreased until complete absence at 10 min, indicating that CRET-NPs were not available for long-term CL imaging of ROS (Fig. 4B).

To investigate the potential of CRET-NPs as a ROS-specific contrast agent, PA images were obtained as a function of time after Ce6-NPs or CRET-NPs were intravenously injected into mice bearing ROS-abundant HT29 tumors. As shown in Fig. 4C, Ce6-NPs as the control did not exhibit considerable PA signal for any of the time tested, which might be due to the low PA quantum yield of Ce6 (*28*). For CRET-NPs, however, a strong PA signal was detected at the tumor site for at least 12 hours, suggesting that CRET-NPs allow long-term ROS imaging in a real-time and noninvasive manner (Fig. 4C). The PA signal reached the maximum at 9 hours, with an 8.6-fold higher intensity from CRET-NPs than from Ce6-NPs (Fig. 4D). To further investigate the performance of PA imaging of the entire tumor region, we displayed multiple line profiles of the signals, extracted from two-dimensional (2D) images containing US and PA images. As shown in Fig. 4E, a 3D-rendered image displayed the PA signal of the CRET-NPs in the entire tumoral region (not limited to the cross-sectional view of the tumor tissue by PA imaging), whereas only weak PA signals were detected in the Ce6-NP–treated group. There was no PA signal from CRET-NPs in normal liver tissue with a low level of ROS (Fig. 4F). Overall, owing to their high specificity to ROS and high PA quantum yield, CRET-NPs allowed collection of prolonged PA image–based geometric information from the entire tumor.

CRET-NPs as a PDT enhancer in vitro

The ROS quantum yield of the photosensitizer has been considered the most important factor for successful treatment of tumors with PDT. In a typical PDT, $^1O_2$ is generated by a type II photochemical reaction as a highly reactive oxygen derivative, leading to cell death via apoptosis or necrosis (*29*). However, because the type II photochemical reaction occurs under normoxic conditions, malignant tumors within a hypoxic region cannot be effectively treated by a conventional photosensitizer (*29*, *30*). Therefore, there is a tremendous need to develop a photosensitizer that can generate cytotoxic ROS through the oxygen-independent type I photochemical reaction. Here, we evaluated the potential of CRET-NPs as a photosensitizer to generate cytotoxic ROS by both type I and type II photochemical reactions based on electron transfer and self-illumination, respectively (Fig. 2, E and F).

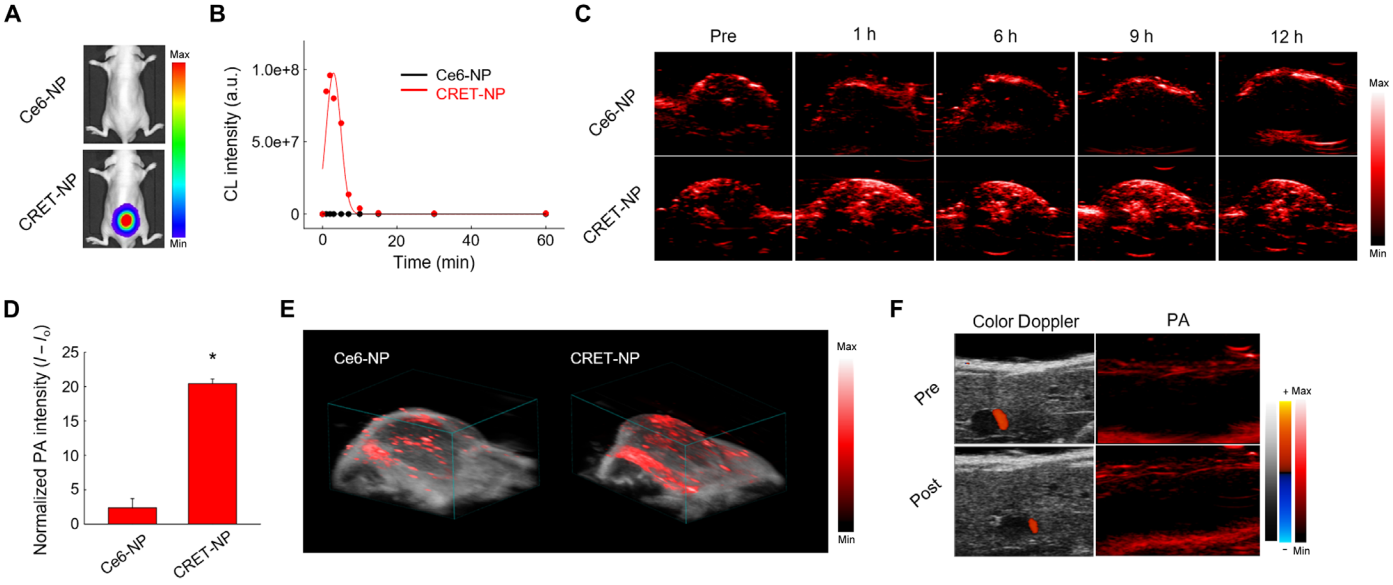

Fig. 4. In vivo PA imaging of CRET-NPs. (**A**) Representative in vivo CL images of Ce6-NPs and CRET-NPs in the presence of H_2O_2. (**B**) CL kinetic profiles of Ce6-NPs and CRET-NPs. (**C**) Time-dependent PA imaging of the tumor site after systemic administration of Ce6-NPs and CRET-NPs. (**D**) Quantification of PA intensities of Ce6-NPs and CRET-NPs. Error bars represent the SD ($n = 3$). *$P < 0.0001$, analyzed by one-way ANOVA. (**E**) 3D-rendered PA images of Ce6-NPs and CRET-NPs. (**F**) Color Doppler images (left) and PA images (right) of liver tissues by CRET-NPs.

To evaluate whether $^1O_2$ could be generated by self-illumination of CRET-NPs, they were used to treat ROS-abundant HT29 colon cancer cells. As shown in Fig. 5A, Ce6-NPs as the control did not generate $^1O_2$ without laser irradiation, whereas CRET-NPs generated a considerable amount of $^1O_2$ even without laser irradiation, implying that self-illumination occurred in response to cellular ROS. Consequently, CRET-NPs exhibited a dose-dependent cytotoxic effect without laser irradiation, whereas no significant cell death was observed for Ce6-NPs (Fig. 5B). On the other hand, upon laser irradiation, the amount of ROS generated from the CRET-NPs, measured using the *p*-nitroso-*N*,*N*′-dimethylaniline (RNO) assay, was significantly higher than that from Ce6-NPs (Fig. 5C). The $-\ln([RNO]_t/[RNO]_o)$ value of CRET-NPs was 2.19-fold higher than that of Ce6-NPs (fig. S11). Owing to their high ROS quantum yield, CRET-NPs exhibited significantly higher cytotoxicity than Ce6-NPs (Fig. 5D). To further examine the photochemical reaction type by CRET-NPs following laser irradiation, $^1O_2$ and free radicals were separately detected as the products of type II and type I photochemical reactions, respectively (Fig. 5, E to G). For electron spin resonance (ESR) spectroscopy, 2,2,6,6-tetramethylpiperide (TMP) and 5,5-dimethyl-1-pyrroline *N*-oxide (DMPO) were used as the trapping agents to detect $^1O_2$ and free radicals, respectively. Upon laser irradiation, the amount of free radicals generated from CRET-NPs was significantly higher than that from Ce6-NPs (Fig. 5E). However, there was no significant difference in the amount of $^1O_2$, produced by the type II photochemical reaction. In addition, for both CRET-NPs and Ce6-NPs, strong signals of singlet oxygen sensor green (SOSG) were detected when they were used to treat HT29 cells in the presence of the laser, indicating that both NPs could effectively generate $^1O_2$ by the type II photochemical reaction (Fig. 5F). The fluorescent signals of free radicals, generated by type I photochemical reaction, were only detected from cells treated with CRET-NPs (Fig. 5G). Overall, it was evident that CRET-NPs were involved in both type I and type II photochemical reactions, enhancing the ROS quantum yield of the photosensitizer (Fig. 5H).

In vivo antitumor efficacy of CRET-NPs

The therapeutic potential of CRET-NPs as a PDT enhancer was investigated after they were intravenously injected into HT29-bearing BALB/c nude mice with or without laser treatment (Fig. 6A). The laser was applied once on day 10 after tumor inoculation. As expected, the groups treated with PBS, free Ce6, and Ce6-NPs showed a marked increase in tumor size without laser treatment (Fig. 6, B and F). On day 25 after inoculation, average tumor volumes with PBS, free Ce6, and Ce6-NPs were 444.00, 381.33, and 358.38 mm^3, respectively. The tumor growth of CRET-NP–treated mice was inhibited to 202.10 mm^3 (Fig. 6B). This might be due to $^1O_2$ generated by site-specific self-illumination of CRET-NPs in ROS-abundant tumor tissue, although complete tumor growth inhibition (CTGI), defined as tumor volume lower than initial (*31*), was not achieved (Figs. 5A and 6F).

For the laser-treated groups, the average tumor volumes tested with PBS, free Ce6, and Ce6-NPs were 369.03, 197.61, and 215.42 mm^3 at 25 days after tumor inoculation, respectively (Fig. 6, C and G). The group treated with CRET-NPs showed a marked decrease in tumor volume to 64.52 mm^3, which might be due to the high level of ROS generated by both type I and type II photochemical reactions (Figs. 5, E to G, and 6C). Consequently, CRET-NPs with laser treatment led to CTGI of the tumor for 60% of mice tested. However, no CTGI of tumors was found in mice treated with PBS, free Ce6, or

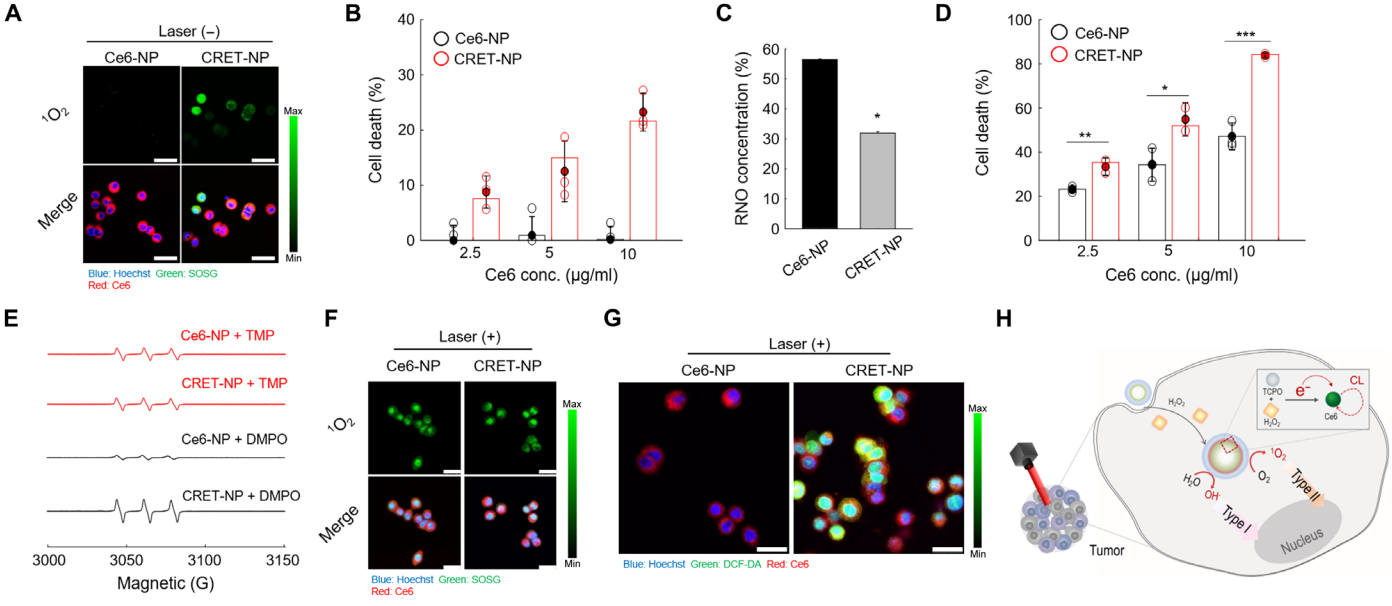

Fig. 5. Characteristics of CRET-NPs as a PDT enhancer. (**A**) Confocal microscopy images of $^1O_2$ (green) and NPs (red) in Ce6-NP–treated and CRET-NP–treated HT29 cells. (**B**) Cytotoxicity of CRET-NPs in HT29 cells. Error bars represent the SD ($n = 4$). (**C**) In vitro ROS generation by Ce6-NPs and CRET-NPs under laser irradiation for 30 min. Error bars represent the SD ($n = 5$). *$P < 0.001$, analyzed by one-way ANOVA. (**D**) Cytotoxicity of PDT with Ce6-NPs and CRET-NPs in HT29 cells. Error bars represent the SD ($n = 5$). *$P < 0.05$, **$P < 0.01$, and ***$P < 0.001$, analyzed by one-way ANOVA. (**E**) ESR spectra of $^1O_2$ and free radicals from Ce6-NPs and CRET-NPs under laser irradiation for 10 min. (**F**) Confocal microscopy images of $^1O_2$ (green) and NPs (red) in Ce6-NP–treated and CRET-NP–treated HT29 cells under laser irradiation. (**G**) Confocal microscopy images of ROS (green) and NPs (red) in Ce6-NP–treated and CRET-NP–treated HT29 cells under laser irradiation. (**H**) Schematic illustration of ROS quantum yield enhancement by CRET-NPs. Scale bars, 25 μm (A, F, and G).

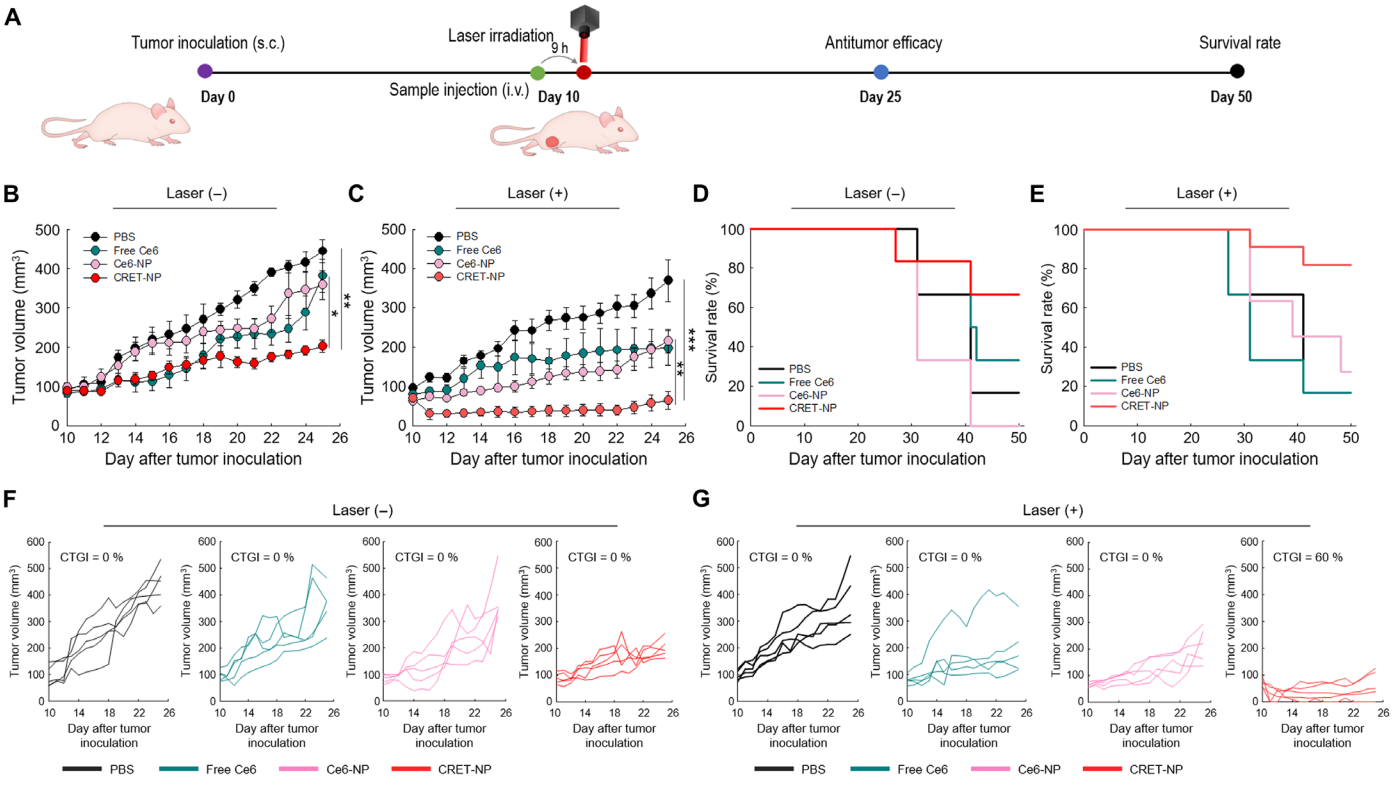

Fig. 6. In vivo therapeutic efficacy of PDT with CRET-NPs. (**A**) Schematic illustration of the treatment regimen of CRET-NP–based PDT. i.v., intravenous; s.c., subcutaneous. (**B** and **C**) Changes in tumor volume by PDT after systemic administration of the samples at 5 mg/kg of Ce6 in HT29 tumor xenograft mice (B) without laser and (C) with laser (635 nm, 50 mW/cm^2) treatment. Error bars represent the SE ($n = 5$). *$P < 0.05$, **$P < 0.01$, and ***$P < 0.001$, analyzed by one-way ANOVA. (**D** and **E**) Survival rate for each treatment group (D) without laser and (E) with laser treatment. (**F** and **G**) Individual tumor growth data and complete regression rate for each treatment group.

Ce6-NPs (Fig. 6G). As shown in Fig. 6 (D and E), the survival rates of CRET-NP–treated mice with and without laser treatment were 82% and 67%, respectively. For the other groups, regardless of laser treatment, the survival rates were less than 40%. Moreover, histological analysis of the major organs of CRET-NP–treated mice showed no sign of toxicity (figs. S12 and S13). Last, upon laser irradiation, the tumors treated with CRET-NPs showed enhanced photodynamic effects compared with the other groups, even with a single treatment (fig. S14).

DISCUSSION

Conventional CRET-NPs have been developed to exhibit characteristics for simultaneous CL imaging and PDT. In general, CL imaging of CRET-NPs has offered outstanding specificity for H_2O_2, along with a high signal-to-noise ratio in vivo (*8*). However, owing to fast consumption of CL donor energy within the nanostructure (*9*), the optical signals of CRET-NPs disappear in a few minutes. This short duration of the CL signal produced by conventional CRET-NPs limits in vivo applications for diagnoses of intractable diseases, such as cancer and rheumatoid arthritis, and inflammatory disorders (*5*, *6*). To overcome such limitations of conventional CRET-NPs, we used a new approach by reinterpreting the hidden nature of CRET (Fig. 1). Here, we designed CRET-NPs, composed of TCPO as a CL donor, Ce6 as a CL acceptor, and PEG-CMD as the hydrophilic polymer shell. Because of their amphiphilic properties with the inner core, consisting of CL donors and acceptors, they had a stable structure with a hydrodynamic size of 128.5 ± 7.48 nm (Fig. 2, A and B).

In the presence of H_2O_2, TCPO is rapidly oxidized to 1,2-dioxetanedione intermediates by the CRET phenomenon, resulting in formation of two CO_2 molecules (Fig. 2D). The CRET-NPs created for this study generated CO_2 for more than 24 hours in the presence of H_2O_2, allowing high PA quantum yield via TEIV (Fig. 3, A to C). PA quantum yield is closely associated with temperature increase and its resulting acoustic wave (*32*). The TEIV by CRET-NPs significantly increased temperature under laser irradiation, compared to thermal expansion or insufficient vaporization (Fig. 3, D to F). This temperature increase by TEIV might originate from the compatibility of thermal expansion by Ce6 and vaporization of CO_2. Consequently, CRET-NPs showed 29-fold higher PA intensity than free Ce6 with a low PA quantum yield ($\Phi_{PA} = 0.036$) (Fig. 3, G to I) (*28*). Because tissues often produce strong background PA signals that can produce false-positive geometric information, use of substances with a high PA quantum yield is essential to obtain accurate information about the disease (*33*). In a tumor-bearing mouse model, CRET-NPs showed significantly higher PA signal intensity at the tumor tissue than Ce6-NPs, solely relying on thermal expansion of Ce6 (Fig. 4, C and D). In addition, sustained CO_2 generation inside CRET-NPs contributed to the prolonged duration of PA signal in vivo. Overall, TEIV-eliciting CRET-NPs might enable authentic molecular imaging using PA in response to ROS-abundant tumor tissue (Fig. 4, E and F).

In recent years, the combination of CL and PDT has been a subject of intense investigation for cancer phototheranostics (*18*). Although CRET-based PDTs have been shown to overcome the depth limitation of conventional PDT, their therapeutic effects are limited by insufficient $^1O_2$, resulting from inadequacy of the emitted CL (*10*, *19*, *20*). In addition, such CRET-based PDTs are not available for hypoxic tumors, because oxygen molecules are essential for the type II photochemical reaction (*29*). Therefore, it is of great interest to develop CRET-based PDTs that can produce hydroxyl radicals by the oxygen-independent type I photochemical reaction. CRET-NPs of this study involved intermolecular electron transfer during CRET for the type I photochemical reaction (Fig. 2F). In addition, they produced a proper wavelength of luminescence (λ_{em} = 670 nm) by resonance energy transfer to activate Ce6 (Fig. 2E). To the best of our knowledge, this is the first demonstration that CRET-NPs can generate an enhanced ROS quantum yield through both electron transfer and self-illumination.

There was no difference between the amount of $^1O_2$ generated by Ce6-NPs and CRET-NPs under laser irradiation (Fig. 5, E and F). Because the efficiency of luminescence photon fluence, produced by self-illuminating agents, is extremely low (~nW level) (*34*), the total amount of $^1O_2$ generated is not significantly affected when coupled with the external light (~mW level) (*35*). In contrast, hydroxyl radicals were generated solely in CRET-NPs (not in Ce6-NPs), possibly due to electron transfer from TCPO to Ce6 during CRET (Fig. 5, E and G). Consequently, the ROS quantum yield of CRET-NPs was much higher than that of Ce6-NPs. Owing to the high ROS quantum yield, CRET-NPs effectively inhibited tumor growth with a CTGI of 60%, even with single administration followed by laser irradiation (Fig. 6, C and G). The hydroxyl radicals produced in the hypoxic region by the type I photochemical reaction might have also contributed to the outstanding therapeutic effect of CRET-NPs.

In summary, we developed CRET-NPs that maintain a stable nanostructure with high PA and ROS quantum yield for cancer phototheranostics. Quantum yield–enhanced CRET-NPs, resulting from the hidden nature of the CRET phenomenon, offer a new phototheranostic modality. Beyond cancer treatment, the findings of this study have broad implications for diagnosis and treatment of intractable diseases using various types of resonance energy transfer, such as Förster resonance energy transfer, bioluminescence resonance energy transfer, and Cerenkov resonance energy transfer.

MATERIALS AND METHODS

Materials

Methoxy polyethylene glycol amine [mPEG-NH_2, molecular weight (M_w) = 5 kDa] was purchased from Laysan Bio Inc. (Alabama, USA). TCPO and sodium cyanoborohydride were purchased from Tokyo Chemical Industry (Tokyo, Japan). CMD sodium salt (M_w = 10 to 20 kDa), *N*-(3-dimethylaminopropyl)-*N*′-ethyl carbodiimide hydrochloride (EDC•HCl), 4-(dimethyl amino)pyridine (DMAP), dimethyl sulfoxide (DMSO), dimethyl formamide (DMF), 2′,7′-dichlorofluorescin diacetate (DCF-DA), TMP, DMPO, and [3-(4,5-dimethylthiazol-2-yl)-2,5-diphenyltetrazolium bromide] (MTT) were purchased from Sigma-Aldrich Co. (St. Louis, MO, USA). The Ce6 was obtained from Frontier Scientific Inc. (Logan, Utah, USA). Human colorectal adenocarcinoma cells (HT29) were purchased from the American Type Culture Collection (Rockville, MD, USA). For cell culture, RPMI 1640 media, antibiotic-antimycotic solution, trypsin-EDTA, and Dulbecco's PBS (DPBS) were purchased from Welgene Inc. (Daegu, Korea). All experiments involving live animals were carried out in accordance with the relevant laws and institutional guidelines of Sungkyunkwan University.

Synthesis of PEG-CMD-Ce6 conjugates

PEG-CMD-Ce6 conjugates were synthesized in a simple two-step procedure, in which mPEG-NH_2 was conjugated to CMD, followed by chemical conjugation of Ce6 to the CMD backbone. mPEG-NH_2 (50 mg, 0.01 mmol) and CMD (150 mg, 0.01 mmol) were dissolved in 0.1 M borate buffer (pH 8.0; 2%, w/v). Afterward, sodium cyanoborohydride (2.52 mg, 0.04 mmol) was added, and the resulting solution was stirred for 4 days at 45°C. The resulting solution was dialyzed against distilled water for 3 days using a dialysis membrane [molecular weight cutoff (MWCO) = 6 to 8 kDa; Spectrum Laboratories Inc., CA, USA], followed by lyophilization. The chemical structure of the mPEG-NH_2–conjugated CMD (mPEG-CMD) was characterized using an ^1H NMR Varian Unity 500 MHz FT-NMR spectrometer (Palo Alto, CA, USA), for which polymer conjugates were dissolved in deuterium oxide (D_2O). Ce6 was chemically conjugated to the CMD backbone via esterification. mPEG-CMD (100 mg, 0.005 mmol) was dissolved in 5 ml of DMSO/distilled water (1:1, v/v) and stirred for 30 min at 25°C. For activation of the carboxyl group of Ce6, Ce6 (19 mg, 0.032 mmol), EDC•HCl (8.05 mg, 0.042 mmol), and DMAP (5.08 mg, 0.042 mmol) were dissolved in 2 ml of DMSO/DMF (1:1, v/v) and stirred for 3 hours in dark conditions at 25°C. The above two solutions were mixed, and the reaction proceeded at room temperature for 24 hours in dark conditions. The PEG-CMD-Ce6 solution was dialyzed against a series of methanol and distilled water (1:1, v/v) and then distilled water for 1 and 2 days sequentially using a dialysis membrane (MWCO = 3.5 kDa). The purified solution was filtered (0.8-mm syringe filter) and lyophilized to obtain a green powder. The chemical structure of PEG-CMD-Ce6 conjugates was confirmed using an ^1H NMR in D_2O/DSMO-d_6 (1:1, v/v).

Preparation of CRET-NPs

To fabricate CRET-NPs, we performed a simple oil-in-water emulsion method as follows: 5 mg of TCPO and 5 mg of PEG-CMD-Ce6 were dissolved in 250 μl of methylene chloride and 125 μl of distilled water, respectively. Each solution was then homogeneously mixed. Afterward, 5 ml of distilled water was added dropwise to the mixture solution with sonication (Sonics Vibra-Cell VCX 750, CT, USA) for 2 min (amplitude: 25%, on: 3 s, off: 1 s). The methylene chloride was evaporated by vigorously stirring in dark conditions.

For in vitro PA imaging studies, we prepared TCPO-bearing NPs for controls (without Ce6 for thermal expansion). In brief, 5β-cholanoamide–conjugated CMD (CMD-CA) was synthesized by chemical conjugation through amide formation; a detailed synthesis procedure is described in (*36*). The control NPs, TCPO-bearing NPs, were prepared by encapsulating TCPO in CMD-CA as described above.

Characterization of CRET-NPs

The hydrodynamic size and zeta potentials of CRET-NPs were measured at a concentration (0.5 mg/ml) in PBS (pH 7.4) using Zetasizer (Nano ZS, Malvern Instruments Ltd., Worcestershire, UK). The morphology of CRET-NPs was observed using high-resolution transmission electron microscopy (HR-TEM; JEOL-2100F, Tokyo, Japan). For TEM analysis, NPs were dropped on a 200-mesh copper

grid and stained with 2 weight % (wt %) uranyl acetate. The EDS mapping images and DPC images were observed by TEM at 200 kV (Talos F200X, FEI Corp., Oregon, USA).

In vitro CL imaging was performed using the In Vivo Imaging System (Lumina Series III, Caliper Life Sciences, Hopkinton, MA, USA) and set up as follows: Ce6-NPs (150 μl) or CRET-NPs (150 μl) were added to each well of a 96-well plate. The concentrations of Ce6 and H_2O_2 were adapted to 1 mg/ml and 100 μM, respectively. Images were obtained with autoexposure time and bioluminescence mode that blocked excitation light. All luminescence images from each well were quantified using embedded software. To analyze emitted CL signals, CL images of CRET-NPs were obtained through various emission filters (520, 570, 620, 670, 710, 790, and 845 nm) in the presence of 100 μM H_2O_2.

CO_2 generation test

In vitro CO_2 generation was performed using a CO_2 titration kit (Sechang Instruments, Korea). TCPO-bearing NPs (10 mg/ml) were diluted 20 times in PBS buffer (pH 7.4). A-1900 activator was then added to the solution for titration. The CO_2 generation test was performed in the presence or absence of 100 μM H_2O_2.

In vitro photothermal effects measurement

To investigate the in vitro photothermal effect of CRET-NPs, 2 ml each of free Ce6, Ce6-NP, TCPO-bearing NP, and CRET-NP solution were exposed to a 635-nm laser (power density: 50 mW/cm^2) for predetermined times. Temperature changes and thermal images were measured by thermometer (TES-1300, TES, Taiwan) and photothermal camera (T430sc, FLIR Systems Inc., Wilsonville, USA), respectively. The rate of temperature change was expressed as the ratio of initial temperature to maximum temperature.

In vitro PA imaging

PA images were obtained by a Vevo LAZR-X (VisualSonics, Toronto, Canada) equipped with an MX550D probe at 40 MHz. For in vitro PA imaging, a 3 wt % agar-gel mold was used for the phantom study. In the phantom study, 300 μl of free Ce6, Ce6-NP, TCPO-bearing NP, and CRET-NP [Ce6 (1 mg/ml), TCPO (1 mg/ml)] solution was used, and in vitro PA imaging was monitored in PA mode (PA gain: 40 dB, 2D gain: 10 dB, depth: 15.00 mm, width: 11.08 mm, sensitivity: high, wavelength: 710 nm). The in vitro PA imaging study was performed in the presence of 100 μM H_2O_2.

In vivo PA imaging

In vivo PA imaging was performed with a Vevo LAZR-X with respiratory anesthesia. In brief, 100 μl of CRET-NPs (5 mg/kg of Ce6, 100 μM H_2O_2) was subcutaneously injected into the lower backs of 6-week-old BALB/c nude mice and monitored as a function of time (fig. S9). To evaluate PA imaging at the tumor site, 200 μl of CRET-NPs and Ce6-NPs at a dose of 5 mg/kg of Ce6 was intravenously injected into HT29 tumor–bearing BALB/c nude mice and monitored as a function of time (Fig. 4, C and E). In vivo PA images of the tumor sites were obtained using PA mode (PA gain: 40 dB, 2D gain: 20 dB, depth: 13.00 mm, width: 12.08 mm, sensitivity: high, wavelength: 710 nm). At each sample, 3D PA images of the tumor site were obtained using stacking B-mode images and PA images. The 3D rendering images were obtained using software for the Vevo LAZR-X (PA gain: 40 dB, 2D gain: 20 dB, depth: 13.00 mm, width: 12.08 mm, sensitivity: high, wavelength: 710 nm, 3D range: 18.69 mm, 3D step size: 0.102 mm).

In vitro ROS generation measurement

In vitro ROS generation by CRET-NPs was estimated by RNO test. An RNO solution was prepared with 5.58 mg of L-histidine and 0.337 μg of *p*-nitroso-*N*,*N*′-dimethylaniline dissolved in 3.8 ml of distilled water. CRET-NPs and Ce6-NPs were dissolved in distilled water [Ce6 (200 μg/ml)]. Then, 200 μl of each sample solution was added to 3.8 ml of RNO solution. Each sample was exposed to a 635-nm laser (50 mW/cm^2) for a predetermined time. The ROS level was measured using a UV/Vis spectrophotometer at 405 nm.

Cell culture

HT29 cells were cultured in RPMI 1640 culture media. All cell growth media were supplemented with FBS (10%), penicillin (100 U/ml), and streptomycin (100 μg/ml), and the cells were cultured at 37°C in a humidified CO_2 incubator.

In vitro phototoxicity assay

First, we investigated the cytotoxicity of CRET-NPs. HT29 cells (2×10^4 cells per well) were seeded onto 96-well plates and incubated for 24 hours. The medium was washed with DPBS, replenished with media containing various concentrations of CRET-NPs, and incubated for a further 24 hours. Cell viability was measured using an MTT assay. To confirm cytotoxicity by PDT in vitro, HT29 cells (2×10^4 cells per well) were seeded onto 96-well plates and incubated for 24 hours. The medium was then replaced with 200 μl of serum-free medium containing CRET-NPs or Ce6-NPs [Ce6 (2.5, 5, or 10 μg/ml)]. After a 9-hour incubation, the cells were washed with DPBS and exposed to a laser (635 nm, 20 mW/cm^2) for 5 min. The cells were incubated at 37°C for 12 hours, and then the MTT assay was performed.

Confocal imaging

The ROS generation of CRET-NPs was investigated using confocal microscopy (TCS SP8 HyVolution, Leica Microsystems CMS GmbH, Germany). To detect singlet oxygen and whole ROS individually, we used SOSG and DCF-DA, respectively. First, we performed singlet oxygen detection in CRET-NP– and Ce6-NP–treated HT29 cells after laser irradiation. In brief, the cells were seeded and incubated for 24 hours. The medium was then replaced with serum-free media containing 10 μM SOSG, followed by incubation at 37°C for 3 hours. Then, CRET-NPs or Ce6-NPs were added and incubated for 1 hour. After exposure to a 635-nm laser for 5 min (20 mW/cm^2), the cells were washed with DPBS, and images were produced by confocal microscopy. To detect whole ROS, HT29 cells were seeded and incubated for 24 hours. Afterward, the cells were incubated with CRET-NPs or Ce6-NPs in serum-free media for 30 min. DCF-DA (10 μM) was then added and incubated for an additional 30 min. After exposure to a 635-nm laser for 5 min (20 mW/cm^2), the cells were washed with DPBS. In situ detection of singlet oxygen and ROS was achieved using a confocal microscope. All cells were stained with Hoechst and imaged by confocal microscopy with diode (405 nm), Ar (514 nm), and He-Ne (633 nm) lasers. To distinguish ROS generation by the type I photochemical reaction, DCF-DA intensity, which indicated whole ROS, was normalized to the basal level of ROS generation by Ce6-NP (Fig. 5G).

In vivo antitumor efficacy

The antitumor efficacy of CRET-NPs was determined by measuring tumor volume as a function of time. HT29 cells (1×10^7) were

injected into the left flank of BALB/c nude mice (6 weeks old, male). After 10 days, when tumor volume reached 50 to 100 mm^3, mice were divided into eight groups: (i) PBS, (ii) free Ce6, (iii) Ce6-NP, (iv) CRET-NP, (v) PBS + laser, (vi) free Ce6 + laser, (vii) Ce6-NP + laser, and (viii) CRET-NP + laser. The injection dose of all was based on Ce6 (5 mg/kg). The laser (635 nm, 50 mW/cm^2, 30 min) was applied 9 hours after systemic administration of each sample. Treatment was performed only once. Tumor volume was calculated as largest diameter × smallest $diameter^2$ × 0.52. Histological analysis was evaluated using hematoxylin and eosin staining. Stained slides (5-μm-thick sections) were observed using a microscope (ScanScope CS, Leica, Germany).

SUPPLEMENTARY MATERIALS

Supplementary material for this article is available at http://advances.sciencemag.org/cgi/content/full/6/21/eaaz8400/DC1

View/request a protocol for this paper from *Bio-protocol*.

REFERENCES AND NOTES

1. D. Lee, S. Khaja, J. C. Velasquez-Castano, M. Dasari, C. Sun, J. Petros, W. R. Taylor, N. Murthy, In vivo imaging of hydrogen peroxide with chemiluminescent nanoparticles. *Nat. Mater.* **6**, 765–769 (2007).
2. X. Huang, L. Li, H. Qian, C. Dong, J. Ren, A resonance energy transfer between chemiluminescent donors and luminescent quantum-dots as acceptors (CRET). *Angew. Chem. Int. Ed.* **45**, 5140–5143 (2006).
3. X. Huang, J. Ren, Nanomaterial-based chemiluminescence resonance energy transfer: A strategy to develop new analytical methods. *TrAC Trend. Anal. Chem.* **40**, 77–89 (2012).
4. C.-K. Lim, Y.-D. Lee, J. Na, J. M. Oh, S. Her, K. Kim, K. Choi, S. Kim, I. C. Kwon, Chemiluminescence-generating nanoreactor formulation for near-infrared imaging of hydrogen peroxide and glucose level in vivo. *Adv. Funct. Mater.* **20**, 2644–2648 (2010).
5. E. S. Lee, V. G. Deepagan, D. G. You, J. Jeon, G.-R. Yi, J. Y. Lee, D. S. Lee, Y. D. Suh, J. H. Park, Nanoparticles based on quantum dots and a luminol derivative: Implications for in vivo imaging of hydrogen peroxide by chemiluminescence resonance energy transfer. *Chem. Commun.* **52**, 4132–4135 (2016).
6. Y.-D. Lee, C.-K. Lim, A. Singh, J. Koh, J. Kim, I. C. Kwon, S. Kim, Dye/peroxalate aggregated nanoparticles with enhanced and tunable chemiluminescence for biomedical imaging of hydrogen peroxide. *ACS Nano* **6**, 6759–6766 (2012).
7. S. Hosaka, T. Itagaki, Y. Kuramitsu, Selectivity and sensitivity in the measurement of reactive oxygen species (ROS) using chemiluminescent microspheres prepared by the binding of acridinium ester or ABEI to polymer microspheres. *Luminescence* **14**, 349–354 (1999).
8. J. Qian, B. Z. Tang, AIE luminogens for bioimaging and theranostics: From organelles to animals. *Chem* **3**, 56–91 (2017).
9. G. Orosz, R. S. Givens, R. L. Schowen, A model for mechanism of peroxyoxalate chemiluminescence as applied to detection in liquid chromatography. *Crit. Rev. Anal. Chem.* **26**, 1–27 (1996).
10. X. Xu, H. An, D. Zhang, H. Tao, Y. Dou, X. Li, J. Huang, J. Zhang, A self-illuminating nanoparticle for inflammation imaging and cancer therapy. *Sci. Adv.* **5**, eaat2953 (2019).
11. P. Beard, Biomedical photoacoustic imaging. *Interface Focus* **1**, 602–631 (2011).
12. J. L. Su, B. Wang, K. E. Wilson, C. L. Bayer, Y.-S. Chen, S. Kim, K. A. Homan, S. Y. Emelianov, Advances in clinical and biomedical applications of photoacoustic imaging. *Expert Opin. Med. Diagn.* **4**, 497–510 (2010).
13. L. M. Lyamshev, Optoacoustic sources of sound. *Soviet Phys. Uspekhi* **24**, 977 (1981).
14. M. W. Sigrist, Laser generation of acoustic waves in liquids and gases. *J. Appl. Phys.* **60**, R83–R122 (1986).
15. K. Wilson, K. Homan, S. Emelianov, Biomedical photoacoustics beyond thermal expansion using triggered nanodroplet vaporization for contrast-enhanced imaging. *Nat. Commun.* **3**, 618 (2012).
16. C. V. Stevani, S. M. Silva, W. J. Baader, Studies on the mechanism of the excitation step in peroxyoxalate chemiluminescence. *Eur. J. Org. Chem.* **2000**, 4037–4046 (2000).
17. S. Kwon, H. Ko, D. G. You, K. Kataoka, J. H. Park, Nanomedicines for reactive oxygen species mediated approach: An emerging paradigm for cancer treatment. *Acc. Chem. Res.* **52**, 1771–1782 (2019).
18. W. Fan, P. Huang, X. Chen, Overcoming the Achilles' heel of photodynamic therapy. *Chem. Soc. Rev.* **45**, 6488–6519 (2016).
19. D. Mao, W. Wu, S. Ji, C. Chen, F. Hu, D. Kong, D. Ding, B. Liu, Chemiluminescence-guided cancer therapy using a chemiexcited photosensitizer. *Chem* **3**, 991–1007 (2017).
20. Y. Zhang, L. Pang, C. Ma, Q. Tu, R. Zhang, E. Saeed, A. E. Mahmoud, J. Wang, Small molecule-initiated light-activated semiconducting polymer dots: An integrated nanoplatform for targeted photodynamic therapy and imaging of cancer cells. *Anal. Chem.* **86**, 3092–3099 (2014).
21. W. Spiller, H. Kliesch, D. Wöhrle, S. Hackbarth, B. Röder, G. Schnurpfeil, Singlet oxygen quantum yields of different photosensitizers in polar solvents and micellar solutions. *J. Porphyr. Phthalocyanines* **2**, 145–158 (1998).
22. S. Kim, T. Y. Ohulchanskyy, D. Bharali, Y. Chen, R. K. Pandey, P. N. Prasad, Organically modified silica nanoparticles with intraparticle heavy-atom effect on the encapsulated photosensitizer for enhanced efficacy of photodynamic therapy. *J. Phys. Chem. C* **113**, 12641–12644 (2009).
23. L. Zhou, S. Wei, X. Ge, J. Zhou, B. Yu, J. Shen, External heavy-atomic construction of photosensitizer nanoparticles for enhanced in vitro photodynamic therapy of cancer. *J. Phys. Chem. B* **116**, 12744–12749 (2012).
24. L. Zhou, X. Ge, J. Liu, J. Zhou, S. Wei, F. Li, J. Shen, Internal heavy atom effect of Au(III) and Pt(IV) on hypocrellin A for enhanced in vitro photodynamic therapy of cancer. *Bioorg. Med. Chem. Lett.* **23**, 5317–5324 (2013).
25. X. Li, N. Kwon, T. Guo, Z. Liu, J. Yoon, Innovative strategies for hypoxic-tumor photodynamic therapy. *Angew. Chem. Int. Ed.* **57**, 11522–11531 (2018).
26. E. Jung, C. Kang, J. Lee, D. Yoo, D. W. Hwang, D. Kim, S.-C. Park, S. K. Lim, C. Song, D. Lee, Molecularly engineered theranostic nanoparticles for thrombosed vessels: H_2O_2-activatable contrast-enhanced photoacoustic imaging and antithrombotic therapy. *ACS Nano* **12**, 392–401 (2018).
27. C. Zong, J. Wu, Y. Zang, H. Ju, Resonance energy transfer and electron–hole annihilation induced chemiluminescence of quantum dots for amplified immunoassay. *Chem. Commun.* **54**, 11861–11864 (2018).
28. C. J. H. Ho, G. Balasundaram, W. Driessen, R. M. Laren, C. L. Wong, U. S. Dinish, A. B. E. Attia, V. Ntziachristos, M. Olivo, Multifunctional photosensitizer-based contrast agents for photoacoustic imaging. *Sci. Rep.* **4**, 5342 (2015).
29. D. E. J. G. J. Dolmans, D. Fukumura, R. K. Jain, Photodynamic therapy for cancer. *Nat. Rev. Cancer* **3**, 380–387 (2003).
30. G. Lan, K. Ni, Z. Xu, S. S. Veroneau, Y. Song, W. Lin, Nanoscale metal–organic framework overcomes hypoxia for photodynamic therapy primed cancer immunotherapy. *J. Am. Chem. Soc.* **140**, 5670–5673 (2018).
31. S. J. Moschos, R. J. Sullivan, W.-J. Hwu, R. K. Ramanathan, A. A. Adjei, P. C. Fong, R. Shapira-Frommer, H. A. Tawbi, J. Rubino, T. S. Rush III, D. Zhang, N. R. Miselis, A. A. Samatar, P. Chun, E. H. Rubin, J. Schiller, B. J. Long, P. Dayananth, D. Carr, P. Kirschmeier, W. R. Bishop, Y. Deng, A. Cooper, G. W. Shipps, B. H. Moreno, L. Robert, A. Ribas, K. T. Flaherty, Development of MK-8353, an orally administered ERK1/2 inhibitor, in patients with advanced solid tumors. *JCI Insight* **3**, e92352 (2018).
32. H. Chen, G. Diebold, Chemical generation of acoustic waves: A giant photoacoustic effect. *Science* **270**, 963–966 (1995).
33. Y.-S. Chen, S. J. Yoon, W. Frey, M. Dockery, S. Emelianov, Dynamic contrast-enhanced photoacoustic imaging using photothermal stimuli-responsive composite nanomodulators. *Nat. Commun.* **8**, 15782 (2017).
34. A. K. Glaser, R. Zhang, J. M. Andreozzi, D. J. Gladstone, B. W. Pogue, Cherenkov radiation fluence estimates in tissue for molecular imaging and therapy applications. *Phys. Med. Biol.* **60**, 6701–6718 (2015).
35. E. C. Pratt, T. M. Shaffer, Q. Zhang, C. M. Drain, J. Grimm, Nanoparticles as multimodal photon transducers of ionizing radiation. *Nat. Nanotechnol.* **13**, 418–426 (2018).
36. M. Lee, H. Lee, N. V. Rao, H. S. Han, S. Jeon, J. Jeon, S. Lee, S. Kwon, Y. D. Suh, J. H. Park, Gold-stabilized carboxymethyl dextran nanoparticles for image-guided photodynamic therapy of cancer. *J. Mater. Chem. B* **5**, 7319–7327 (2017).

Acknowledgments

Funding: This work was financially supported by the Basic Science Research Programs (2018R1D1A1B07049447 and 2018R1A2B3006080) of the National Research Foundation (NRF), Republic of Korea. **Author contributions:** D.G.Y. and J.H.P. designed the research and conducted the data analysis. J.J., D.G.Y., S.K., and J.H.P. wrote the manuscript. J.J. performed most of the experiments. W.U., J.L., C.H.K., and S.S. performed the in vivo animal tests. **Competing interests:** The authors declare that they have no competing interests. **Data and materials availability:** All data needed to evaluate the conclusions in the paper are present in the paper and/or the Supplementary Materials. Additional data related to this paper may be requested from the authors.

Submitted 14 October 2019
Accepted 6 March 2020
Published 20 May 2020
10.1126/sciadv.aaz8400

Citation: J. Jeon, D. G. You, W. Um, J. Lee, C. H. Kim, S. Shin, S. Kwon, J. H. Park, Chemiluminescence resonance energy transfer–based nanoparticles for quantum yield–enhanced cancer phototheranostics. *Sci. Adv.* **6**, eaaz8400 (2020).